Chemical pressure effect on magnetic properties in electron-doped perovskite manganites $(Gd_{0.08}Ca_ySr_{0.92-y})MnO_3$ $(0<y<1)$: Percolation transition of ferromagnetic clusters

Shingo Hirano,* Jun Sugiyama,† Tatsuo Noritake, and Toshihiko Tani
Toyota Central Research and Development Laboratories, Inc., Nagakute, Aichi 480-1192, Japan
(Received 10 June 2003; revised manuscript received 20 February 2004; published 24 September 2004)

The magnetic properties of electron-doped perovskite manganites, $(Gd_xCa_ySr_{1-x-y})MnO_3$ ($x=0.08$ and 0.05, $0.1\leqslant y<1$), were investigated as a function of the average ionic radius of the *A*-site cations (i.e., Gd, Ca and Sr), $\langle r_A\rangle$using polycrystalline samples. For the samples with $x=0.08$, as y increased from 0, the low temperature phase changed from an antiferromagnetic insulator (AFI) to a ferromagnetic metal (FM) at $y\sim0.35$ which corresponds to $\langle r_A\rangle=1.25$ Å. The magnitude of the Néel temperature was found to correlate with the bandwidth of the Mn−3*d* band. On the other hand, for the samples with $y>0.5$, a small saturation magnetization suggested the coexistence of the FM and AFI phase; in other words, magnetic phase separation occurred below the Curie temperature (~120 K). A scaling analysis of the resistivity of $(Gd_{0.08}Ca_ySr_{0.92-y})MnO_3$ indicated that a percolation transition between FM clusters was induced by the decrease in $\langle r_A\rangle$.

DOI: 10.1103/PhysRevB.70.094419 PACS number(s): 75.47.Lx, 75.30.Kz, 75.30.Cr, 61.10.Nz

I. INTRODUCTION

Doped perovskite manganites $RE_xAE_{1-x}MnO_3$ (RE denotes a trivalent rare earth ion and AE a divalent alkaline earth ion, henceforth both are called as *A*-site cations) have been studied extensively because of their colossal magnetoresistance (CMR) effect.[1] Recent studies regarding the hole-doped manganites have revealed two crucial parameters that govern the relationship between their crystal structure, magnetism, and electrical transport properties. One is a charge-carrier doping; for example, e_g-electrons are introduced by chemical substitution for AE^{2+} by RE^{3+}. This causes a ferromagnetic (F) metallic state in which the itinerant e_g-electrons mediate an F double-exchange interaction.[2,3] The other is an effective one-electron bandwidth (W), which is affected strongly by the degree of the hybridization between Mn-3*d* and O-2*p* orbitals. The magnitude of W is controlled by the average ionic radius of the *A*-site cations ($\langle r_A\rangle$), i.e., the chemical pressure,[4–7] which induces the evolution of the F transition temperature (T_C) for the hole-doped manganites. Other factors, including temperature and applied (physical) pressure, provide various magnetic phase diagrams for the hole-doped manganites.[8–10]

The electron-doped manganites, $RE_xSr_{1-x}MnO_3$, $RE_xCa_{1-x}MnO_3$, and $Bi_xCa_{1-x}MnO_3$ ($x<0.5$), etc. have been studied recently because of their peculiar magnetic properties, including magnetic phase separation and the CMR effect.[11–23] As with the hole-doped manganites, magnetic phase diagrams in the electron-doped manganites depend strongly on $\langle r_A\rangle$.[13] Unlike the hole-doped manganites, the CMR effect in the electron-doped manganites is observed only in a narrow region in a phase diagram. For example, $RE_{1-x}Ca_xMnO_3$ ($x>0.5$) exhibits the CMR effect at around the critical concentration x_c (~0.8–0.9).[11,12] Charge ordering phenomena together with antiferromagnetic (AF) ordering state are observed for $x<x_c$, while F metallic state appears for $x>x_c$. The competition between charge ordering, the AF ordering and the F metallic phenomena leads to the CMR effect at the phase boundary of $x=x_c$. Thus, the coexistence of both magnetic phases is important for the CMR effect in the electron-doped manganites. For the hole-doped manganites, there are many reports regarding the chemical pressure effect on various physical properties,[4,6,7,24,25] which provide important information about their magnetic phase separation behavior. To the best of our knowledge, however, there has been no detailed report on the effect of chemical pressure on magnetotransport properties of the electron-doped manganites.

We have investigated the effect of chemical pressure on the magnetic and electrical properties of the electron-doped manganites $(Gd_xCa_ySr_{1-x-y})MnO_3$ ($x=0.08$ and 0.05, $0.1\leqslant y<1$) to understand the physical nature of magnetic phase separation and to clarify the ground-state phase evolution in detail. According to our preliminary experiments using several rare earth oxides, the sample with the highest density was easily obtained using Gd_2O_3. We therefore selected Gd as a dopant for the current work to elucidate the change in the transport properties by chemical pressure.

II. EXPERIMENT

Polycrystalline samples of $(Gd_xCa_ySr_{1-x-y})MnO_3$ ($x=0.08$ and 0.05, $0.1\leqslant y<1$) were synthesized by a conventional solid-state reaction from stoichiometric mixtures of Gd_2O_3, $CaCO_3$, $SrCO_3$, and Mn_2O_3. The mixtures were calcined at 1573 K for 12 h in air, then sintered at 1823 K for 5 h in air. The heating and the cooling rate of the sintering process were ~100 and 200 K/h, respectively. Densities of the sintered samples were ~92% of the theoretical values. Powder x-ray diffraction XRD (Cu-$K\alpha$ radiation, model RINT-1500V, *RIGAKU*, 40 kV, 350 mA) analysis was used to determine the crystal structure at room temperature. Structural parameters were refined by the Rietveld method using the program RIETAN 2000.[26] The value of $\langle r_A\rangle$ was calculated using the tabulated values for cations in a ninefold coordination.[27]

Electrical resistivity (ρ) was measured using a standard dc four-probe method in the temperature range between 25 and

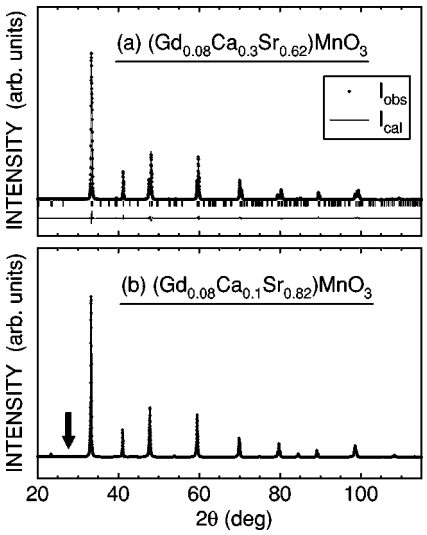

FIG. 1. (a) A powder x-ray diffraction pattern and the result of the Rietveld analysis for $(Gd_{0.08}Ca_{0.3}Sr_{0.62})MnO_3$, and (b) a powder x-ray diffraction pattern for $(Gd_{0.08}Ca_{0.1}Sr_{0.82})MnO_3$. In (b), the arrow indicates a very weak diffraction peak probably due to the hexagonal perovskite phase.

300 K. Magnetic susceptibility (χ) from 5 to 600 K was measured using a superconducting quantum interference device (SQUID) magnetometer (mpms, *Quantum Design*) in a magnetic field H of less than 55 kOe. Hall voltage was measured at 300 K using an ac four-probe technique with $H \leqslant 60$ kOe (ppms, *Quantum Design*) for thin plate samples with ~ 200 μm thickness.

III. RESULTS AND DISCUSSION

A. Crystal structure

The $(Gd_{0.08}Ca_ySr_{0.92-y})MnO_3$ samples with $y \geqslant 0.2$ were assigned to be single-phase of the orthorhombic-perovskite structure with the *Pnma* space group [Fig. 1(a)], in which the MnO_6 octahedra are rotated around and tilted off the b axis. The sample with $y=0.1$ was almost single-phase of the orthorhombic-perovskite structure, while a very small amount of the hexagonal-perovskite phase was detected in the XRD pattern [Fig. 1(b)], as in the case of $Pr_{0.1}Sr_{0.9}MnO_3$.[14] However, the diffraction intensity of the peaks from the hexagonal phase was extremely weak compared with that from the main phase [actually, almost invisible in Fig. 1(b)]. We therefore ignored the contribution from the hexagonal phase in the structural analysis using the Rietveld method.

Although a cubic- or a tetragonal-perovskite phase was reported to be stabilized in the Sr-rich manganites due to an increase in $\langle r_A \rangle$,[14,23,28] the current XRD patterns for the samples with $y \leqslant 0.5$ were well fitted using the orthorhombic-perovskite structure and were unable to be fitted using the cubic- and/or the tetragonal-perovskite structure.

The refined structural parameters determined by the Rietveld analysis for the $(Gd_{0.08}Ca_ySr_{0.92-y})MnO_3$ samples with $y \geqslant 0.1$ are listed in Tables I and II. Figure 2 shows the variation in the structural parameters as a function of Ca content y for $(Gd_{0.08}Ca_ySr_{0.92-y})MnO_3$. The unit cell volume ($V$) decreases monotonically with increasing y, as expected from the difference between the ionic radii of Sr^{2+} and Ca^{2+}. A similar change in the cell volume with increasing Ca content has also been reported for polycrystalline $(Ca,Sr)MnO_3$ samples.[28] For the orthorhombic perovskite, the coordination number of the Mn ions is six; however, there are two unequivalent oxygen sites, which are named the O(1) and O(2) sites in the unit cell [two oxygen atoms locate on the O(1) site and the rest four on the O(2) site]. Namely, there are three Mn-O bonds (d_{Mn-O}) and two Mn-O-Mn angles (θ), which are determined by the direction of the crystallographic axis.

Although the three d_{Mn-O} are almost independent of y, the values of $d_{Mn-O,ac1}$ and $d_{Mn-O,ac2}$ for the samples with $y=0.7$ and 0.8 seem to deviate from such behavior. Since the accuracy of the atomic positions for the samples with $y=0.7$ and 0.8 is approximately equal to that for the other samples, this would indicate the difficulties for determining the oxygen positions using the powder XRD data. Nevertheless, the average of the three d_{Mn-O} is almost independent of y and in good agreement with the result for the orthorhombic perovskite $CaMnO_3$ ($d_{Mn-O} \sim 1.9$ Å) determined by a neutron powder diffraction analysis.[19,20] On the other hand, the two Mn-O-Mn bond angles are found to decrease systematically with increasing y [see Fig. 2(c)]. The implications of the variation in these parameters are discussed later. However, it

TABLE I. Refined structural parameters determined by the Rietveld analysis of the powder x-ray diffraction pattern (Cu-$K\alpha$ radiation) for the $(Gd_{0.08}Ca_ySr_{0.92-y})MnO_3$ samples with $y \geqslant 0.1$.

Ca content y	a (Å)	b (Å)	c (Å)	V (Å^3)	R_{wp} (%)	R_I (%)	S
0.1	5.3722(2)	7.6207(3)	5.3729(2)	219.97(1)	9.91	2.65	2.78
0.2	5.3548(1)	7.6279(1)	5.3555(2)	218.75(0)	7.15	2.48	1.92
0.3	5.3383(1)	7.6294(2)	5.3396(2)	217.47(0)	7.14	2.02	1.87
0.4	5.3623(3)	7.5501(3)	5.3420(3)	216.28(2)	12.96	2.91	1.27
0.5	5.3503(2)	7.5437(3)	5.3335(2)	215.27(1)	9.02	4.39	1.98
0.7	5.3127(1)	7.5152(2)	5.3175(1)	212.30(1)	10.46	4.73	1.25
0.8	5.3053(1)	7.4961(2)	5.3005(1)	210.79(1)	8.33	4.44	1.73
0.92	5.3010(1)	7.4731(2)	5.2797(1)	209.16(1)	12.35	5.66	1.34

TABLE II. Atomic positions determined by the Rietveld analysis of the powder x-ray diffraction pattern (Cu-$K\alpha$ radiation) for the $(Gd_{0.08}Ca_ySr_{0.92-y})MnO_3$ samples with $y \geqslant 0.1$; the position of Mn is (0,0,0.5) for all samples.

	Ca/Sr/Gd			O(1)			O(2)		
Ca content y	x	y	z	x	y	z	x	y	z
0.1	0.001(7)	0.25(0)	−0.003(4)	0.49(5)	0.25(0)	0.03(2)	0.26(4)	−0.01(2)	−0.24(4)
0.2	0.001(5)	0.25(0)	−0.006(1)	0.50(3)	0.25(0)	0.027(7)	0.26(1)	−0.005(5)	−0.263(6)
0.3	0.001(4)	0.25(0)	−0.007(1)	0.50(2)	0.25(0)	0.036(6)	0.26(1)	0.01(1)	−0.26(2)
0.4	0.005(2)	0.25(0)	−0.001(3)	0.489(8)	0.25(0)	0.055(5)	0.264(6)	0.013(4)	−0.264(6)
0.5	0.008(2)	0.25(0)	0.001(5)	0.480(7)	0.25(0)	0.03(1)	0.272(5)	0.026(4)	−0.269(5)
0.7	0.0217(4)	0.25(0)	−0.002(2)	0.491(2)	0.25(0)	0.059(5)	0.290(2)	0.025(2)	−0.261(4)
0.8	0.0273(5)	0.25(0)	−0.006(2)	0.490(2)	0.25(0)	0.069(5)	0.270(4)	0.026(2)	−0.292(2)
0.92	0.0337(5)	0.25(0)	−0.007(1)	0.492(2)	0.25(0)	0.066(4)	0.284(2)	0.027(2)	−0.285(2)

should be pointed out here that the linear relationship between V and y is caused by not the shrinkage of d_{Mn-O}, but by the deviations of θ from 180° (i.e., the tilting of the MnO_6 octahedra).

B. Antiferromagnetic phase

Both magnetic and transport properties of $(Ca,Sr)MnO_3$ are reported to depend on $\langle r_A \rangle$, i.e., the chemical pressure.[28] Furthermore, the parent compounds of the current system, $CaMnO_3$ and $SrMnO_3$, are an antiferromagnetic insulator with the Néel temperature T_N of 123 and 233 K, respectively.[28] The magnitude of T_N for $(Gd_{0.08}Ca_ySr_{0.92-y})MnO_3$ is therefore expected to be strongly affected by y (i.e., $\langle r_A \rangle$), if they are also antiferromagnetic. Thus, at first, we focus on the effect of chemical pressure on the AF transition in $(Gd_{0.08}Ca_ySr_{0.92-y})MnO_3$.

Figure 3 shows the $\chi(T)$ curves measured in the field-cooled mode with $H=10$ kOe for the $(Gd_{0.08}Ca_ySr_{0.92-y})MnO_3$ samples with $y \leqslant 0.5$. The maxima in the $\chi(T)$ curves indicate the AF transition with $T_N = 150-255$ K. Here, the value of $\langle r_A \rangle$ of the samples indicating the AF transition ranges from 1.23 to 1.28 Å, as in the case of $(Sm,Sr)MnO_3$.[13] For the samples with $y > 0.5$, the magnitude of χ dramatically increases with decreasing T especially below ~120 K (Fig. 4), indicating the existence of a F phase with $T_C \sim 120$ K. In addition, the magnitude of χ below T_C increases with increasing y.

Assuming that only Mn^{3+}, Mn^{4+}, and Gd^{3+} moments are responsible for the paramagnetic behavior of χ at temperatures above T_N or T_C, the Curie-Weiss law in the general form is written as

$$\chi = \frac{N_{Mn}\mu^2_{eff,Mn} + N_{Gd}\mu^2_{eff,Gd}}{3k_B(T-\Theta_p)} + \chi_0, \quad (1)$$

where N_{Mn} and N_{Gd} are the number density of Mn and Gd ions (per unit gram), $\mu_{eff,Mn}$ and $\mu_{eff,Gd}$ are the effective magnetic moment of Mn and Gd ions, k_B is the Boltzmann's constant, T is the absolute temperature, Θ_p is the paramagnetic Curie temperature, and χ_0 is the temperature-independent susceptibility. Using Eq. (1) over the temperature range between 300 and 600 K and $\mu_{eff,Gd}=7.80\ \mu_B$, we can obtain the values for $\mu_{eff,Mn}$, Θ_p, and χ_0 for the $(Gd_{0.08}Ca_ySr_{0.92-y})MnO_3$ samples, as listed in Table III. T_N was simply defined as the peak temperature in the $\chi(T)$ curve.

As y increases from 0, Θ_p decreases up to $y=0.3$, suddenly changes the sign from negative to positive near $y=0.35$, and then increases with further increases in y (see Fig. 5), indicating that the magnetic phase boundary exists at $y \sim 0.35$. Ignoring the data for the $y=0.2$ and 0.3 samples, $\mu_{eff,Mn}$ is almost independent of y ($\sim 3.7\ \mu_B$), as shown in Table III; this value is in good agreement with the spin only moment of Mn ions for $(Gd_{0.08}Ca_ySr_{0.92-y})MnO_3$ ($3.94\ \mu_B$). The AF interaction, therefore, weakens with increasing y, and the F interaction is dominant for the samples with $y \geqslant 0.4$, while the electron configuration of the Mn ions is unaffected by the Ca substitution for Sr.

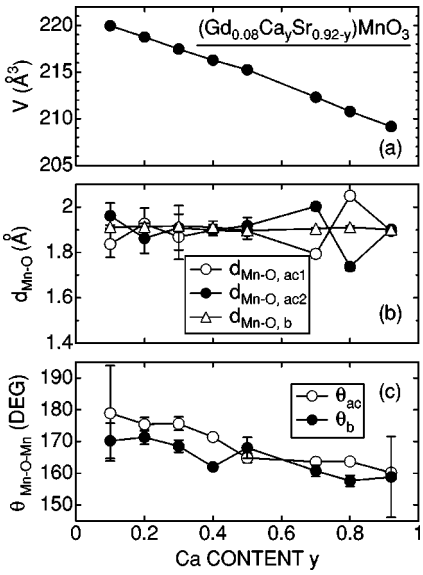

FIG. 2. Structural parameters of $(Gd_{0.08}Ca_ySr_{0.92-y})MnO_3$ as a function of the Ca content y; (a) unit cell volume, (b) Mn-O bond length, and (c) Mn-O-Mn bond angle. In (b), $d_{Mn-O,ac1}$ and $d_{Mn-O,ac2}$ are the Mn-O bond lengths in the ac plane.

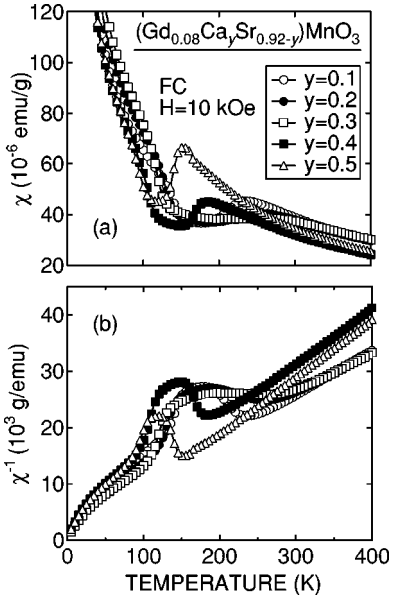

FIG. 3. Temperature dependences of (a) χ and (b) χ^{-1} for $(Gd_{0.08}Ca_ySr_{0.92-y})MnO_3$ with $y \leqslant 0.5$; χ was measured in the field-cooled mode with $H=10$ kOe.

The magnitudes of $\mu_{\mathrm{eff,Mn}}$ for the $y=0.2$ and 0.3 samples are larger by $\sim 0.6\ \mu_B$ than those for the others. Also, the sign of χ_0 for the samples with $y=0.2$ and 0.3 is negative, while that for the others positive. Although the magnitude of χ_0 is expected to be independent of y, the observed variation of χ_0 seems to be strongly related to that of Θ_p, which apparently changes the sign around $y=0.35$. On the other hand, the anomaly in $\mu_{\mathrm{eff,Mn}}$ (and the accompanying decrease in χ_0) suggests that the magnetic phase boundary exists at $y \sim 0.35$. Thus, this indicates that both anomalies in $\mu_{\mathrm{eff,Mn}}$ and χ_0 would be induced by critical phenomena caused by the competition between the F and AF interaction, although the details are not fully understood. By contrast, a long-range F order is observed for the samples with $y > 0.5$ (see Figs. 3 and 4), suggesting that the remaining AF interaction suppresses the long-range F order in the samples with $y \leqslant 0.5$.

Figure 6 shows the temperature dependences of resistivity ρ and $d(\ln \rho)/d(T^{-1}) \times k_B$, (i.e., the activation energy, E) below 300 K for the $(Gd_{0.08}Ca_ySr_{0.92-y})MnO_3$ samples. For the samples with $y=0.4$ and 0.5, $\rho(T)$ increases remarkably below T_N with decreasing temperature. This indicates that the AF ordering induces an insulating behavior in the electron-doped manganites. The $E(T)$ curves exhibit maxima at $T_{\max}$ [see Fig. 6(b)] and the highest value of $T_{\max}$ (=225 K) is observed for the sample with $y=0.3$. It is worth noting that the highest T_N was also observed for the samples with $y=0.3$. The $\rho(T)$ curves for the samples with $y \leqslant 0.3$ exhibit a semiconducting behavior over a wide temperature range, although $\rho(T)$ for the samples with $y > 0.3$ shows a metallic behavior in the paramagnetic state. Since the value of n_H is almost independent of y $2.0-2.7 \times 10^{21}$ cm^{-3}, as seen in Table III), the metallic behavior for the samples with $y > 0.3$ is concluded to be induced by a decrease in . This suggests the formation of F clusters in the AF matrix, as discussed below.

Assuming that one Mn^{3+} ion produces one electron in the current manganites, the measured n_H provides the Mn^{3+} content as 0.10–0.14, which is larger than that expected from the Gd content, i.e., ~ 0.08. This indicates the existence of oxygen deficiency δ (=0.01–0.03) in the $(Gd_{0.08}Ca_ySr_{0.92-y})MnO_{3-\delta}$ samples.

Next, we discuss the correlation between T_N and crystal structure for the samples with $x=0.08$ and $0 < y \leqslant 0.5$. As y increases from 0 to 0.3, T_N increases up to 255 K and then decreases with further increasing y above 0.3. Note that this behavior looks to correlate with $T_{\max}$ (see Table III). The variation of T_N in the undoped perovskite manganites, $Ca_ySr_{1-y}MnO_3$ and $Ba_ySr_{1-y}MnO_3$, was discussed using the following two factors; i.e., the *A*-site ionic size variance (σ^2) and the spatial average of $\theta_{\mathrm{Mn\text{-}O\text{-}Mn}}$ (θ_{av}) in the orthorhombic lattice.[28,29] Both are expressed as

$$\sigma^2 = \Sigma y_i r_i^2 - \langle r_A \rangle^2, \tag{2}$$

$$\cos^2 \theta_{\mathrm{av}} = \frac{\cos^2 \theta_{\mathrm{Mn\text{-}O(1)\text{-}Mn}} + 2\cos^2 \theta_{\mathrm{Mn\text{-}O(2)\text{-}Mn}}}{3}, \tag{3}$$

where y_i and r_i are the fractional occupancy and the ionic radius of the ith cations in the *A*-site. The two angles $\theta_{\mathrm{Mn\text{-}O(1)\text{-}Mn}}$ and $\theta_{\mathrm{Mn\text{-}O(2)\text{-}Mn}}$ are caused by the orthorhombic

TABLE III. Magnetic and transport parameters for $(Gd_{0.08}Ca_ySr_{0.92-y})MnO_3$. That is, the paramagnetic Curie temperature Θ_p, the effective magnetic moment of Mn ions $\mu_{\mathrm{eff,Mn}}$, the temperature-independent susceptibility χ_0, the maximum temperature in the $E(T)$ curve $T_{\max}$ (see Fig. 6) and the carrier concentration n_H estimated from Hall measurements at 300 K.

Ca content y	T_N or T_C (K)	Θ_p (K)	μ_{eff} (μ_B/Mn ion)	χ_0 ($\times 10^{-3}$ emu/mol)	$T_{\max}$ (K)	n_H ($\times 10^{21}$ cm^{-3})
0.1	235	−23±9	3.69±0.09	0.09±0.10	218	2.0±0.8
0.2	255	−69±8	4.24±0.08	−0.46±0.09	219	2.5±0.2
0.3	255	−88±20	4.36±0.18	−0.58±0.19	225	2.3±0.6
0.4	185	23±7	3.37±0.07	0.32±0.08	176	2.3±0.1
0.5	150	21±9	3.56±0.09	0.08±0.10	144	2.7±0.5
0.7	~120	49±4	3.36±0.04	0.25±0.05		2.1±0.6
0.8	~120	54±7	3.52±0.08	0.16±0.10		2.5±0.3
0.92	~120	66±3	3.39±0.04	0.19±0.05		2.0±0.3

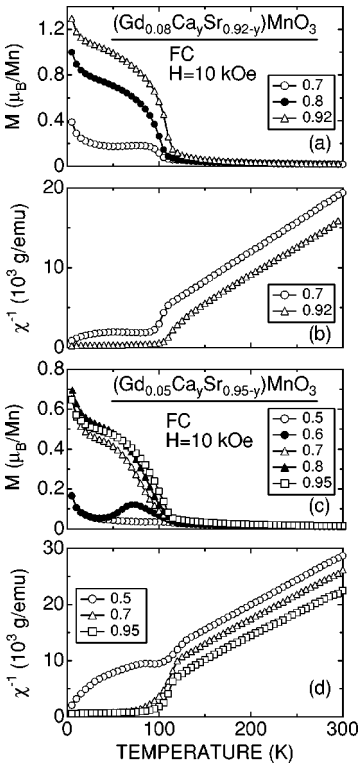

FIG. 4. Temperature dependencies of (a) magnetization M and (b) χ^{-1} for $(Gd_{0.08}Ca_ySr_{0.92-y})MnO_3$ with $y>0.5$; and (c) M and (d) χ^{-1} for $(Gd_{0.05}Ca_ySr_{0.95-y})MnO_3$ with $y \geq 0.5$.

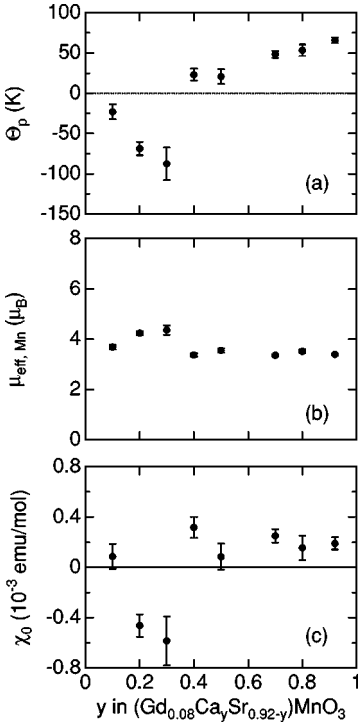

FIG. 5. (a) The paramagnetic Curie temperature, Θ_p, (b) the effective magnetic moment of Mn ions, $\mu_{\mathrm{eff,Mn}}$ and (c) the temperature-independent susceptibility, χ_0 as a function of y for $(Gd_{0.08}Ca_ySr_{0.92-y})MnO_3$.

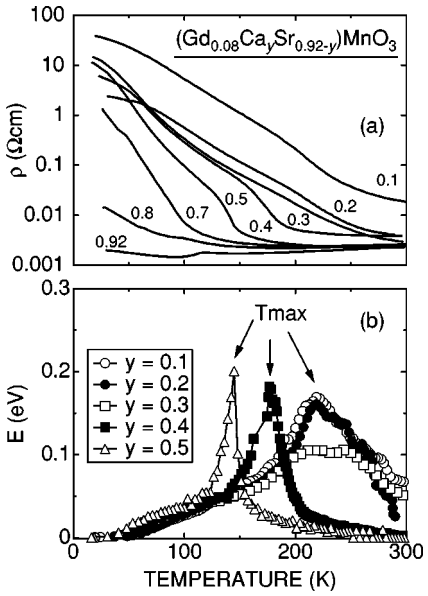

FIG. 6. Temperature dependence of (a) resistivity ρ and (b) $d(\ln \rho)/d(T^{-1}) \times k_B$ (i.e., the activation energy, E) for $(Gd_{0.08}Ca_ySr_{0.92-y})MnO_3$.

distortion of the unit cell. This model was successful to explain the decrease in T_N with y in $Ca_ySr_{1-y}MnO_3$ and $Ba_ySr_{1-y}MnO_3$.[28] On contrary, the magnitude of T_N increases with y up to 0.3 in the current Gd-doped manganites, as seen in Table III. This indicates that the above model is unavailable for $(Gd_{0.08}Ca_ySr_{0.92-y})MnO_3$.

We therefore focus on the effect of the hybridization between Mn-3d and O-2p orbitals on the AF transition in the $(Gd_{0.08}Ca_ySr_{0.92-y})MnO_3$ samples. For the orthorhombic perovskite manganites, the effective band width W is represented within the tight-binding approximation

$$W \propto \frac{\cos \omega}{d_{\mathrm{Mn\text{-}O}}^{3.5}}, \tag{4}$$

where ω is the tilt angle in the MnO_4 plane and is given by $\omega = 0.5(\pi - \theta_{\mathrm{Mn\text{-}O\text{-}Mn}})$ and $d_{\mathrm{Mn\text{-}O}}$ is the Mn-O bond length.[6,30] Figure 7 shows the variation in T_N and the relative W ($W_r = W(y)/W(y=0.1)$) as a function of for $(Gd_{0.08}Ca_ySr_{0.92-y})MnO_3$. Although the accuracy of W_r is relatively low due to the analytical errors of the Mn-O-Mn angles and Mn-O bond lengths, the W_r-$\langle r_A \rangle$ curve seems to exhibit a broad maximum at $\langle r_A \rangle \sim 1.25$ Å (i.e., $y=0.3$), as in the case of the hole-doped manganites.[6] The maximum of W_r in Fig. 7 is mainly induced by a slight decrease in the average Mn-O bond length at $y=0.3$. Furthermore, both the T_N-$\langle r_A \rangle$ and T_{max}-$\langle r_A \rangle$ curve are found to show a broad maximum at $\langle r_A \rangle \sim 1.26$ Å (Figs. 6 and 7, and Table III). These results suggest that W is the suitable parameter for explaining the change in T_N for the current manganites, because the structural, magnetic, electrical transport properties are strongly coupled to each other. In other words, the superexchange interaction between the neighboring Mn ions is affected by the hybridization between Mn-3d and O-2p orbitals.

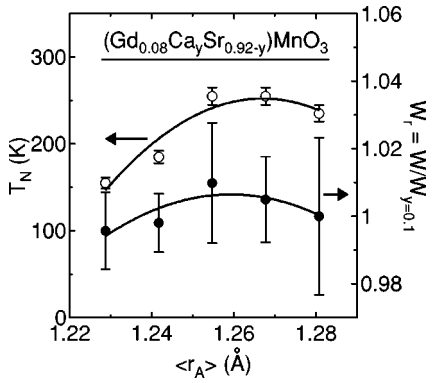

FIG. 7. The magnitude of T_N and the relative W ($W_r = W(y)/W(y=0.1)$) as a function of for $(Gd_{0.08}Ca_ySr_{0.92-y})MnO_3$ with $y \leqslant 0.5$.

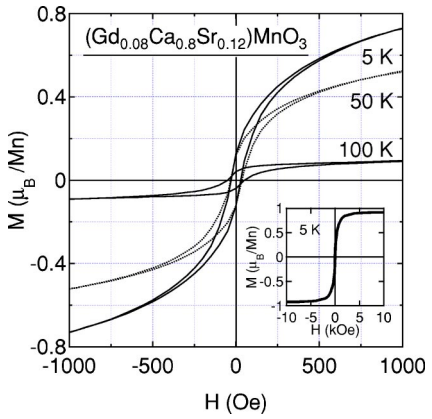

FIG. 8. The relationship between M and H for $(Gd_{0.08}Ca_{0.8}Sr_{0.12})MnO_3$ at 5, 50, and 100 K under $H \leqslant 1000$ Oe. The inset shows the M-H curve at 5 K under $H \leqslant 10$ kOe.

In the above discussion, we ignored the temperature dependence of the crystal structure. To understand the chemical pressure effect on magnetism in fully detail, both neutron and x-ray diffraction studies as a function of temperature are necessary.

C. Ferromagnetic transition and phase separation

The transition from the paramagnetic state to the F state is clearly observed at $\sim$120 K ($=T_C$) for the $(Gd_{0.08}Ca_ySr_{0.92-y})MnO_3$ samples with $y \geqslant 0.7$ and $(Gd_{0.05}Ca_ySr_{0.95-y})MnO_3$ with $y \geqslant 0.6$ [Figs. 4(a)–4(d)]. The increase in the Gd content leads the enhancement of M below T_C, as in the case of the electron-doped $La_xCa_{1-x}MnO_3$ with $x \leqslant 0.1$, in which electrons are doped into the AF band insulator $CaMnO_3$.[15,18] Furthermore, the magnitude of M below T_C increases with increasing y, whereas ρ below T_C decreases (Fig. 6). These are well explained by the decrease in the AF interaction between Mn ions caused by the shrink of .

Figure 8 shows the relationship between M and H for $Gd_{0.08}Ca_{0.8}Sr_{0.12}MnO_3$ at 5, 50, and 100 K. Assuming the paramagnetic behavior of the Gd ions in the sample, we subtracted the contribution of the Gd moment from the measured M. A clear M-H loop is observed below T_C, although the saturation magnetization (M_s) is rather small ($\sim$0.9 μ_B/Mn ion at 5 K); in addition, the coercive field H_c appears to be independent of T ($H_c \sim 50$ Oe) below 100 K. A similar result was also obtained for $Gd_{0.05}Ca_ySr_{0.95-y}MnO_3$. If the Mn moments are in the fully F ordered state, $M_s \sim 3$ μ_B/Mn ion, as in the case of $CaMnO_3$. Therefore, the small M_s indicates that part of the samples exhibited ferromagnetism. Since the magnetism of the sample changes from AF to F with increasing chemical pressure, our result suggests that F clusters are distributed in the AF matrix phase, as reported for several electron-doped manganites.[16–18,20–22] Machida *et al.* reported that two magnetic phases coexisted in $Tb_{0.1}Ca_{0.9}MnO_3$ on a nanometer scale (i.e., F and G-type AF phases).[20,22] Furthermore, recent specific heat measurements on $Tb_xCa_{1-x}MnO_3$ suggested charge separation behavior,[21] which was anticipated theoretically for the double-exchange-interaction system with a low electron density.[31] In fact, our recent μSR studies on $Gd_{0.08}Ca_ySr_{0.92-y}MnO_3$ ($y > 0.5$) suggested an inhomogeneous distribution of the internal magnetic field even at 5 K.[32]

Since the coexistence of AF and F phases was not observed in the $Pr_xSr_{1-x}MnO_3$ ($x \leqslant 0.15$) samples,[14] such behavior is also unlikely to exist in the Ca-poor $Gd_{0.08}Ca_ySr_{0.92-y}MnO_3$ samples. On the other hand, the values of Θ_p and M at 5 K increased systematically with y for the samples with $y > 0.5$; these facts and the small M_s observed for the samples with $y > 0.5$ suggest that the fraction of F clusters increases with y. We therefore conclude that the F metallic clusters are distributed randomly in the AF matrix phase in the Ca-rich samples. In such cases, a percolation transition between the separated F clusters would occur at a certain temperature below T_C, inducing a change from an insulating to a metallic state (see Fig. 6). Within the percolation theory, a power law gives a total resistivity of a composite, which consists of an insulator and a conductor

$$\rho \propto (C - C_c)^{-t}, \tag{5}$$

where ρ is the bulk resistivity of the sample, C is the concentration of the conductive component, C_c is the percolation threshold concentration, and t is the critical exponent.[33–35]

Figure 9 shows the relationship between $\log \rho$(30 K) and $\log(y - y_c)$ for $Gd_{0.08}Ca_ySr_{0.92-y}MnO_3$ with $y \geqslant 0.7$. Here, the critical concentration $y_c = 0.6$ was determined from the dependence of M(5 K) on y. That is, as y increases from 0, M(5 K) increases rapidly above $\sim$0.6, whereas almost 0 below 0.6 (see the inset of Fig. 9). Note that, above y_c, ρ(30 K) changes by about 3 orders of magnitude and the logarithm of ρ is almost proportional to that of $(y - 0.6)$. Using Eq. (7) and $C = y$, we obtain the resistivity critical exponent t as 5.4. This value is smaller than that reported for the hole-doped manganites $La_{5/8-y}Pr_yCa_{3/8}MnO_3$ ($t = 6.9$),[25] whereas rather larger than the universal exponent in the three dimensional percolation theory ($t \simeq 2$).[33] The enhancement of t for the hole-doped manganites is well explained by the percolative conduction through metallic regions embedded in insulating regions.[25] Our scaling analysis therefore suggests that

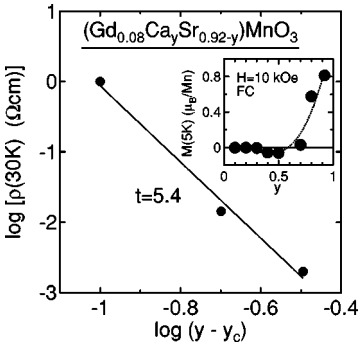

FIG. 9. The relationship between $\rho(30\ \mathrm{K})$ and $(y-0.6)$ for the samples with $y \geqslant 0.7$; the absolute value of the slope is equivalent to the resistivity critical exponent t. The inset shows $M(5\ \mathrm{K})$ as a function of y for $(Gd_{0.08}Ca_ySr_{0.92-y})MnO_3$.

the percolative phase separation also occurs in $Gd_{0.08}Ca_ySr_{0.92-y}MnO_3$, and the F phase is distributed randomly in the AF matrix. This is consistent with the fact that T_C is independent of y for the samples with $0.7 \leqslant y \leqslant 0.92$. In other words, the F cluster model is reasonable for understanding magnetism in $Gd_{0.08}Ca_ySr_{0.92-y}MnO_3$.

Conversely, $M(5\ \mathrm{K})$ is found to be level off to a constant value ($\sim 0.65\ \mu_B$/Mn ion) for $Gd_{0.05}Ca_ySr_{0.95-y}MnO_3$ with $y \geqslant 0.7$ [see Fig. 4(c)]. This is probably because the carrier concentration ($x=0.05$) is too close to the critical concentration of x for the metal-insulator transition induced by an electron doping. As a result, the magnetic properties of the electron-doped manganites are quite sensitive to both x and y.

IV. SUMMARY

We investigated the magnetic properties of electron-doped perovskite manganites $(Gd_xCa_ySr_{1-x-y})MnO_3$ ($x=0.08$ and 0.05, $0 \leqslant y < 1$). The average ionic radius of the A-site cations was found to have a significant effect on the transport properties and magnetism of $(Gd_xCa_ySr_{1-x-y})MnO_3$. For the samples with $x=0.08$, the boundary between the antiferromagnetic insulator AFI and the ferromagnetic metal FM phases was located near ~ 1.25 Å($y \sim 0.35$). The scaling analysis of resistivity indicated that the FM clusters are distributed randomly in the AFI matrix. The metal-insulator transition at ~ 1.22 Å($y \sim 0.6$) was explained as a percolation transition between the FM clusters.

ACKNOWLEDGMENTS

We would like to acknowledge Professor J. H. Brewer of University of British Columbia and Professor E. J. Ansaldo of TRIUMF for their helpful discussions using the μSR results. Also, we would like to thank Dr. R. Asahi of Toyota CRDL and Professor N. Kamegashira of Toyohashi Institute of Technology for their fruitful discussions.

*Present address: Department of Materials Engineering, Graduate School of Engineering, University of Tokyo, 7-3-1 Hongo, Bunkyo-ku, Tokyo 113-8656, Japan.
†Electronic address: e0589@mosk.tytlabs.co.jp

[1] See, *Colossal Magnetoresistance, Charge Ordering and Related Properties of Manganese Oxide*, edited by C. N. R. Rao and B. Raveau (World Scientific, Singapore, 1998).
[2] C. Zener, Phys. Rev. **82**, 403 (1951).
[3] P. W. Anderson and H. Hasegawa, Phys. Rev. **100**, 675 (1955).
[4] H. Y. Hwang, S-W. Cheong, P. G. Radaelli, M. Marezio, and B. Batlogg, Phys. Rev. Lett. **75**, 914 (1995).
[5] Y. Tomioka, H. Kuwahara, A. Asamitsu, M. Kasai, and Y. Tokura, Appl. Phys. Lett. **70**, 3609 (1997).
[6] P. G. Radaelli, G. Iannone, M. Marezio, H. Y. Hwang, S-W. Cheong, J. D. Jorgensen, and D. N. Argyriou, Phys. Rev. B **56**, 8265 (1997).
[7] H. Yoshizawa, R. Kajimoto, H. Kawano, Y. Tomioka, and Y. Tokura, Phys. Rev. B **55**, 2729 (1997).
[8] Y. Moritomo, A. Asamitsu, and Y. Tokura, Phys. Rev. B **51**, 16491 (1995).
[9] Y. Moritomo, H. Kuwahara, and Y. Tokura, J. Phys. Soc. Jpn. **66**, 556 (1997).
[10] Y. Moritomo, H. Kuwahara, Y. Tomioka, and Y. Tokura, Phys. Rev. B **55**, 7549 (1997).
[11] H. Chiba, M. Kikuchi, K. Kusaba, Y. Muraoka, and Y. Syono, Solid State Commun. **99**, 499 (1996).
[12] A. Maignan, C. Martin, F. Damay, and B. Raveau, Chem. Mater. **10**, 950 (1998).
[13] C. Martin, A. Maignan, M. Hervieu, and B. Raveau, Phys. Rev. B **60**, 12 191 (1999).
[14] M. Hervieu, C. Martin, A. Maignan, G. Van Tendeloo, Z. Jirák, J. Hejtmánek, A. Barnabé, D. Thopart, and B. Raveau, Chem. Mater. **12**, 1456 (2000).
[15] J. J. Neumeier and D. H. Goodwin, J. Appl. Phys. **85**, 5591 (1999).
[16] C. Martin, A. Maignan, M. Hervieu, B. Raveau, Z. Jirák, M. M. Savosta, A. Kurbakov, V. Trounov, G. André, and F. Bourée, Phys. Rev. B **62**, 6442 (2000).
[17] M. M. Savosta, P. Novák, M. Maryško, Z. Jirák, J. Hejtmánek, J. Englich, J. Kohout, C. Martin, and B. Raveau, Phys. Rev. B **62**, 9532 (2000).
[18] J. J. Neumeier and J. L. Cohn, Phys. Rev. B **61**, 14 319 (2000).
[19] J. Blasco, C. Ritter, J. García, J. M. de Teresa, J. Pérez-Cacho, and M. R. Ibarra, Phys. Rev. B **62**, 5609 (2000).
[20] A. Machida, Y. Moritomo, K. Ohoyama, and A. Nakamura, J. Phys. Soc. Jpn. **70**, 3739 (2001).
[21] Y. Moritomo, A. Machida, E. Nishibori, M. Takata, and M. Sakata, Phys. Rev. B **64**, 214409 (2001).
[22] A. Machida, Y. Moritomo, S. Mori, N. Yamamoto, K. Ohoyama, E. Nishibori, M. Takata, M. Sakata, T. Otomo, and A. Nakamura, J. Phys. Soc. Jpn. **71**, 27 (2002).
[23] O. Chmaissem, B. Dabrowski, S. Kolesnik, J. Mais, J. D. Jorgensen, and S. Short, Phys. Rev. B **67**, 094431 (2003).
[24] Y. Moritomo, Phys. Rev. B **60**, 10374 (1999).

[25] M. Uehara, S. Mori, C. H. Chen, and S.-W. Cheong, Nature (London) **399**, 560 (1999).
[26] F. Izumi and T. Ikeda, Mater. Sci. Forum **321–324**, 198 (2000).
[27] R. D. Shannon, Acta Crystallogr., Sect. A: Cryst. Phys., Diffr., Theor. Gen. Crystallogr. **32**, 751 (1976).
[28] O. Chmaissem, B. Dabrowski, S. Kolesnik, J. Mais, D. E. Brown, R. Kruk, P. Prior, B. Pyles, and J. D. Jorgensen, Phys. Rev. B **64**, 134412 (2001).
[29] L. M. Rodriguez-Martinez and J. P. Attfield, Phys. Rev. B **54**, R15 622 (1996).
[30] M. Medarde, J. Mesot, P. Lacorre, S. Rosenkranz, P. Fischer, and K. Gobrecht, Phys. Rev. B **52**, 9248 (1995).
[31] M. Y. Kagan, D. I. Khomskii, and M. V. Mostovoy, Eur. Phys. J. B **12**, 217 (1999).
[32] J. Sugiyama, J. H. Brewer, E. J. Ansaldo, S. Hirano, H. Itahara, and T. Tani, Physica B **329-333**, 902 (2003).
[33] *Applications of Percolation Theory*, edited by M. Sahimi (Taylor & Francis, London, 1994).
[34] I. Balberg, Phys. Rev. Lett. **59**, 1305 (1987).
[35] M. B. Heaney, Phys. Rev. B **52**, 12 477 (1995).